Chemical Science

Accepted Manuscript

This article can be cited before page numbers have been issued, to do this please use: X. Luo, J. Liu, X. Zhou, Y. Lei, L. Wang, D. Jiang and Y. Zhuo, *Chem. Sci.*, 2026, DOI: 10.1039/D6SC01141A.

ROYAL SOCIETY OF CHEMISTRY

rsc.li/chemical-science

View Article Online
DOI: 10.1039/D6SC01141A

ARTICLE

Multi-Responsive Tetrahedral DNA Frameworks for In-Situ Methyltransferase Imaging to Distinguish Living Chemoresistant Tumor Cells

Received 00th January 20xx,
Accepted 00th January 20xx

DOI: 10.1039/x0xx00000x

Xin-Yu Luo,[a] Jie Liu,*[a] Xue-Mei Zhou,[a] Yan-Mei Lei,[a] Lu-Xi Wang,[a] De-Peng Jiang*[b] and Ying Zhuo*[a]

Chemoresistance, a primary contributor to approximately 90% of cancer-related deaths, stems from the tumor cells' ability to endure chemotherapy-induced DNA methylation damage via aberrant upregulation of DNA repair enzymes, such as O^6-methylguanine-DNA methyltransferase (MGMT). Herein, we report a multi-responsive tetrahedral DNA framework (Mr-TDF) that enables accurate distinguishing of chemoresistant tumor cells through in situ and highly sensitive imaging of MGMT activity in living cells. The Mr-TDF incorporates four identical multi-responsive DNAzyme probes (Mr) anchored on a DNA tetrahedral scaffold, with each probe integrating three key modules: MGMT recognition, DNAzyme activation and fluorescent signal output. Upon MGMT-mediated demethylation of the O^6-methylguanine lesion on Mr probe, the DNAzyme's catalytic activity is specifically reactivated, resulting in rA-site cleavage and subsequent fluorescence signal generation. Leveraging the spatial confinement effect of the DNA tetrahedral scaffold, the Mr-TDF achieves highly sensitive and rapid monitoring of MGMT activity, producing fluorescence signals more than three times stronger in chemoresistant tumor cells compared to that of chemosensitive counterparts. This study establishes a robust platform for probing epigenetic dynamics in living chemoresistant cells and offers new avenues for mechanistic investigations and early diagnosis of chemoresistance.

Introduction

Active surveillance of chemoresistance is essential for improving clinical efficacy in cancer therapy[1,2]. Currently, most methods for assessing chemoresistance rely on genomic/transcriptomic analyses and protein-expression assays such as mRNA quantification, immunohistochemistry, and enzyme-linked immunosorbent assay[3-5]. These approaches generally demand specialized sequencing equipment[6], extensive experimental procedures[7], and destructive processing procedures[8], which lead to the loss of spatial and temporal information and poor compatibility with in situ cellular analysis. More importantly, macroscopic changes in genomic alterations and mRNA levels cannot directly and accurately reflec[9-11], thereby limiting their translational potential for timely clinical decision-making.

Epigenetic plasticity, a dynamic and multilayered regulatory process, is a central driver of chemoresistance, because it modulates base-level chemical modifications that reprogram gene expression without altering the underlying DNA sequence[12-14]. For instance, alkylating chemotherapeutic agents induce DNA damage that triggers apoptosis[15], whereas chemoresistant tumor cells evade this effect through enhanced DNA repair activitys[16,17]. In particular, O^6-methylguanine-DNA methyltransferase (MGMT) directly contributes to chemoresistance by removing alkyl adducts from the O^6-methylguanine lesions[18,19], thereby serving as a predictive biomarker of chemoresistance[20-22]. Conventional methods such as ELISA can quantitatively assess MGMT via antigen–antibody interactions[23,24], however, their limited sensitivity and inability to resolve intracellular localization restrict their use for analyzing MGMT in living cells.

Advances in DNA molecular engineering have enabled the development of DNAzyme modules[25], which leverage inherent programmability and catalytic turnover to overcome the limitations of conventional biosensing technologies, positioning them as a powerful platform for intracellular applications[26-28]. For example, by rationally engineering methylation-responsive sites within DNAzymes, one can achieve dynamic tracking of MGMT activity in living cells[29]. However, conventional linear duplex DNAzymes[30,31] are hindered by poor cellular uptake efficiency and short intracellular retention, which impede

[a]*MOE Key Laboratory of Luminescence Analysis and Molecular Sensing, College of Chemistry and Chemical Engineering, Institute of Developmental Biology and Regenerative Medicine, Southwest University, Chongqing 400715, P R China. E-mail: jieliu20256051@swu.edu.cn (J.Liu) ; yingzhuo@swu.edu.cn (Y.Zhuo)*
[b]*Department of Respiratory Medicine, The Second affiliated Hospital of Chongqing Medical University, Chongqing 400010, P R China. E-mail: qdp116@hospital.cqmu.edu.cn (D.P.Jiang)*
† Electronic Supplementary Information (ESI) available: Experimental section and related experimental data. See DOI: 10.1039/x0xx00000x

accurate detection of low-abundance targets. Furthermore, free molecular diffusion restricts the encounter efficiency between sparse DNAzyme species and their targets, resulting in a significant slowdown of the sensor's kinetic response. In contrast, DNA frameworks with rigid ordered three-dimensional structure exhibit robust cellular internalization and high intracellular stability, serving as scalable scaffolds for precise anchoring of functional probes at vertex sites[32,33]. This architecture not only extends probe internalization and retention, but also creates a confined nanoscale environment that increases local probe concentration. With this knowledge in mind, it is considered that incorporating DNAzyme modules into a DNA tetrahedron scaffold represents a promising strategy for rapid, sensitive in situ visualization and selective recognition of low-abundance MGMT in cancer cells.

In this work, we developed a multisite-responsive tetrahedral DNA framework (Mr-TDF) based fluorescent biosensor for real-time and sensitive imaging of MGMT in living cells, which enabled efficient distinction of chemoresistance in glioblastoma cells. The Mr-TDF integrates four identical multi-responsive DNAzyme probes (Mr) precisely anchored at the vertices of a tetrahedral DNA scaffold. Each probe couples an O^6-methylguanine-modified DNAzyme domain for MGMT recognition with a hairpin substrate module for fluorescence signal output. This innovative design not only enhances the intracellular delivery and retention of Mr probes, but also accelerates reaction kinetics toward MGMT, thereby facilitating real-time monitoring of MGMT activity in living cells.

Results and discussion

Design and Construction of Mr-TDF for Monitoring MGMT Activity

The Mr-TDF frameworks integrate four identical **m**ulti-**r**esponsive DNAzyme probes (Mr) within a **t**etrahedral **D**NA **f**ramework (TDF), as depicted in Scheme 1A. Each Mr probe serves as a sensing element for MGMT and consists of two functional domains: (i) an O^6-methylguanine-modified DNAzyme (Me-DNAzyme) unit, whose catalytic activity can be restored through MGMT-mediated demethylation, and (ii) a hairpin (H0) unit containing an rA site and a fluorescent donor-quencher pair of FAM-BHQ1 for signal output. The TDF acts as a nanocarrier, anchoring the four Mr probes to provide high stability and accelerate reaction kinetics for MGMT detection. As illustrated in Scheme 1B, the enzymatic activity of Me-DNAzyme within the Mr-TDF is initially suppressed by the O^6-methylguanine inhibitory group, keeping the H0 fluorescence quenched. Upon the presence of MGMT, the O^6-methylguanine inhibitory group is removed, thereby reactivating the DNAzyme to cleave H0 substrate and generate a strong fluorescence signal. This cascade enables in situ spatial imaging of MGMT activity and accurate discrimination of chemoresistant tumor cells (Scheme 1C).

To validate the structure of the Mr-TDF framework, we assembled a tetrahedral DNA hairpin complex by anchoring four H0 hairpins onto TDF via base-pair hybridization, with the resultant assembly denoted as TDH. As illustrated in Fig. 1A, the TDH construction involves two main processes. The TDF is first formed by annealing

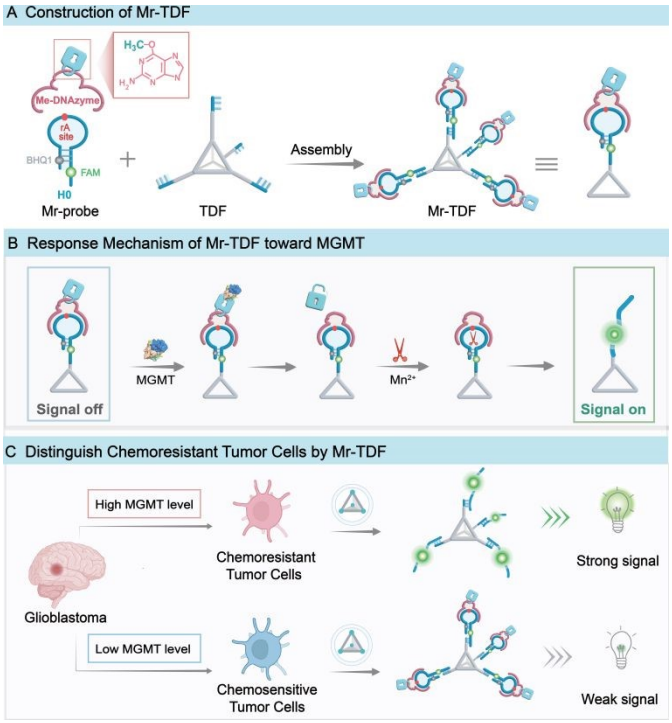

Scheme 1. Schematic illustration of the Mr-TDF frameworks for sensitive and selective imaging of MGMT in chemoresistant tumor cells. (A) Design and construction of Mr-TDF using multifunctional probes and DNA tetrahedron. (B) Working principle of the Mr-TDF for fluorescent imaging of MGMT. (C) Application of Mr-TDF for distinguishing chemoresistant and chemosensitive tumor cells.

four single stranded DNAs (T1-T4). Subsequently, the H0 hairpins are hybridized to the TDF vertices. Before the preparation of TDH, the formation of hairpin H0 was optimized under optimal annealing temperature and duration to minimize dimer formation and the detailed annealing process is shown in Fig. S1. The assembly process of TDH was confirmed using PAGE. As shown in Fig. 1B, lane 1 displayed a single band corresponding to the single-stranded DNA T1. Sequential addition of T2, T3, and T4 in lanes 2 to 4 resulted in progressively slower migration rates, indicating the stepwise formation of intermediate DNA assemblies. Notably, lane 4 showed a brighter band with the lowest mobility, confirming the complete assembly of the TDF. After incubating H0 with the TDF, lane 5 displayed a distinct band with even slower migration, verifying successful hybridization of the H0 hairpins. Furthermore, atomic force microscopy (AFM) was employed to characterize the TDH dimensions. The bare TDF particles had a height of 3-4 nm (Fig. 1C and 1E), while TDF particles hybridized with H0 showed an increased height of 5 nm (Fig. 1D and 1F), which was consistent with the theoretical expectations for TDH. Collectively, these results demonstrated the successful formation of the TDH structure.

View Article Online
DOI: 10.1039/D6SC01141A

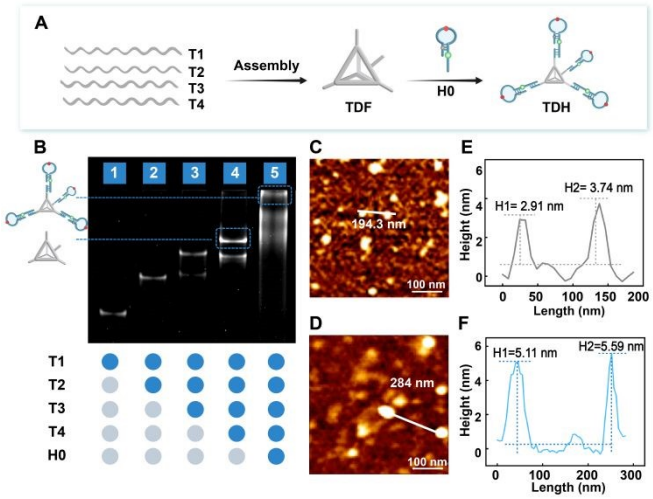

Fig. 1 Construction and characterization of TDH. (A) Assembly process of the TDH. (B) PAGE analysis for characterization the assembly process of TDH. (C, D) AFM image of the TDF (C) and TDH (D) particles. (E, F) AFM cross-sectional profiles of the TDF (E) and TDH (F) particles highlighted by white lines in the corresponding AFM images.

Feasibility Assessment of Mr-TDF for Monitoring MGMT Activity

As illustrated in Fig. 2A, Mr-TDF was designed to selectively capture MGMT through a cascade mechanism, in which MGMT demethylates the DNAzyme to restore its catalytic activity, subsequently triggering cleavage of the H0. The feasibility of Mr-TDF for detecting MGMT activity was evaluated using PAGE (Fig. 2B). The individual H0 hairpin and DNAzyme strand without O^6-methylguanine modification displayed distinct bands in lanes 1 and 2, respectively. When H0 was mixed with the unmodified DNAzyme strand in the absence of Mn^{2+}, no new band appeared in lane 3. However, upon adding Mn^{2+} into this mixture, a diffuse band in lane 4 with faster mobility than intact H0 strand was observed, indicating that H0 could be cleaved by the unmodified DNAzyme strand. In lane 5, the Me-DNAzyme strand displayed a distinct band with migration similar to that of unmodified DNAzyme strand in lane 2. Following incubation with MGMT, the mixture of Me-DNAzyme strand and H0 in lane 6 revealed distinct bands at lower positions, matching the cleavage products seen in lane 4, which suggests that the MGMT induces demethylation of the Me-DNAzyme strand, thereby restoring its catalytic activity to cleave H0. In contrast, without MGMT treatment, the mixture in lane 7 displayed a bright, intact H0 band, confirming that the O^6-methylguanine modification effectively inhibits the catalytic activity of the Me-DNAzyme strand. These PAGE results collectively demonstrated that MGMT presence is necessary to restore the DNAzyme's activity and enable H0 cleavage. Subsequently, fluorescence spectroscopy was employed to assess the responsivity of Mr-TDF for MGMT activity detection (Fig. 2C). The pH of reaction buffer (20 mM Tris-HCl, 20 mM NaCl) was first optimized, and pH 7.5 was identified and used in all subsequent experiments (Fig. S2). As depicted in Fig. 2D, a pronounced fluorescence signal was observed upon incubation of Mr-TDF with MGMT, while only a low background signal was detected without MGMT. Statistical analysis revealed a significant difference between the two groups (P = 1.33 × 10^{-4}, unpaired t test), thereby confirming the feasibility and reliability of Mr-TDF for MGMT detection.

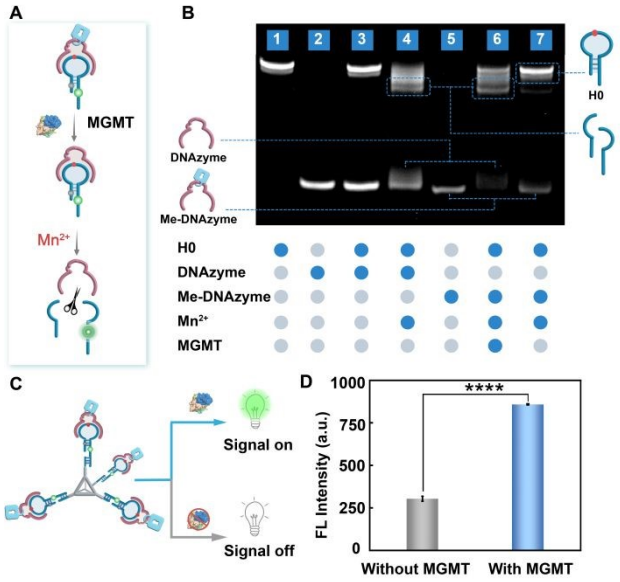

Fig. 2 Feasibility verification of Mr-TDF for MGMT detection. (A) Schematic illustration of the MGMT-mediated activation of DNAzyme and the subsequent cleveage of H0 in Mr-TDF. (B) PAGE characterization of the DNAzyme cleavage reaction regulated by MGMT. (C) Schematic illustration of the reaction process of Mr-TDF for MGMT detection. (D) Fluorescence responses of Mr-TDF with MGMT and without MGMT in reaction buffer at 37 °C for 2 h. Error bars are shown as mean ± SD (n = 3). Statistical significance was calculated via Student's t test. $^{****}P < 0.0001$.

Reaction Kinetics of Mr-TDF for MGMT Activity Detection

To investigate the spatial confinement effect of Mr-TDF system, we compared the reaction kinetics of the confined Mr-TDF and free Mr probes with equivalent amounts of MGMT-responsive modules using real-time fluorescence measurements (Fig. 3A and 3B). As shown in part II of Figure 3C, upon incubation with MGMT, the free Mr porbes displayed a slow increase in fluorescence signal, whereas the Mr-TDF system exhibited a rapid and sustained signal elevation. Based on a previously reported kinetic model[34], the reaction rate constant (k) for Mr-TDF system was calculated as 2.291 × 10^{-3} M^{-1} s^{-1} ,which was 1.8 times higher than that of the free Mr probes. As the reaction microenvironment and total concentration of MGMT-responsive modules were kept identical in the free Mr and Mr-TDF systems, we further examined whether the kinetic enhancement was associated with substrate binding affinity. Surface plasmon resonance (SPR) analysis showed that MGMT exhibited comparable K_d values toward free Mr and Mr-TDF (Fig. S3). This indicates that tetrahedron confinement had a little effect on substrate affinity, which can be explained by the fact that the overall structure of the responsive modules on Mr-TDF remains essentially unchanged with that of free Mr. Subsequently, to investigate the underlying mechanism for this kinetic enhancement, collision theory was employed to estimate the local concentration and corresponding reaction volume using the equation V = 1/cN. As illustrated in part I of Fig. 3C, the average

reaction volume of the free Mr probes at 100 nM was estimated to be 1.66 × 10^{-17} L. As expected, with the introduction of the tetrahedral DNA frameworks, the reaction volume was reduced to 4.95 × 10^{-20} L, resulting in a local probe concentration of 33.5 μM, a 335-fold increase compared to the free-diffusing Mr system (Fig. 3D, Part I). Collectively, these findings demonstrated that the nanoscale spatial confinement provided by TDF significantly enhances the local concentration of Mr probes, thereby accelerating the cascade reaction kinetics.

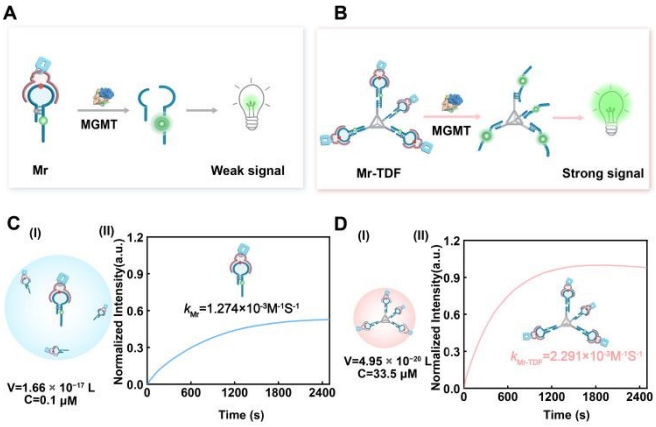

Fig. 3 Verification the reaction kinetics of Mr-TDF for monitoring of MGMT activity. (A, B) Schematic illustration of the sensing mechanism for free Mr probes system (A) and Mr-TDF frameworks system (B). (C, D) Normalized real-time fluorescence intensity profiles for free Mr probes system (C) and Mr-TDF frameworks system (D) upon addition of 1 μM MGMT in reaction buffer at 37 °C for 2 h.

Analytical Performance of Mr-TDF for Monitoring MGMT Activity

To assess the analytical performance of Mr-TDF in MGMT activity sensing, a series of fluorescence experiments were systematically performed. As shown in Fig. 4A, the fluorescence intensity was gradually increased with the increase of MGMT concentrations from 0 nM to 3.16 × 10^3 nM, displaying a positive correlation between MGMT activity and fluorescence intensity. Additionally, a well-defined linear correlation within the concentration range of 1-1000 nM was established between fluorescence intensity (*I*) and the logarithm of MGMT concentration (lg *c*), following the regression equation *I* = 250 lg*c* + 475 with the correlation coefficient *R* of 0.9978 (Fig. 4B). Meanwhile, the limit of detection (LOD) was calculated to be as low as 0.31 nM. Compared with previously reported MGMT sensors, our Mr-TDF exhibits broader linear range and lower detection limit (Table S1). Moreover, the selectivity of the Mr-TDF system toward MGMT activity detection was further evaluated with four representative interfering substances (AlkB, FTO, UDG, and hAAG). As shown in Fig. 4C, in contrast to the strong fluorescence signal derived from MGMT, the signals induced by these interfering substances were negligible, even when their concentrations were 100-fold higher than MGMT, demonstrating that high selectivity of the Mr-TDF toward MGMT. To evaluate the capability of Mr-TDF for screening MGMT inhibitors, O^6-benzylguanine (O^6-BG), a structural analog of O^6-alkylguanine that irreversibly inactivates MGMT via active-site alkylation, was employed as a model inhibitor. As shown in Fig. 4D, with the increase of O^6-BG concentration, MGMT activity detected by the Mr-TDF probe was gradually decreased. The half-maximal inhibitory concentration (IC_{50}) was calculated to be 359 nM, consistent with previously reported values (273 nM)[31]. These results demonstrated that the Mr-TDF not only enables sensitive and selective detection of MGMT activity but also serves as a promising platform for screening potential MGMT inhibitors. Furthermore, the free probe (Mr) exhibited noticeable degradation after 2 h and was almost completely degraded after 6 h in 10% fetal bovine serum (FBS), whereas Mr-TDF displayed remarkable structural stability, with no obvious degradation observed even after 24 h incubation (Fig. S4). In addition, Mr-TDF maintained a stable functional imaging window of approximately 8 h inside cells (Fig. S5). These results demonstrate that the tetrahedral DNA framework significantly enhances the biostability of the Mr-TDF, thereby ensuring its structural integrity in subsequent living cell imaging.

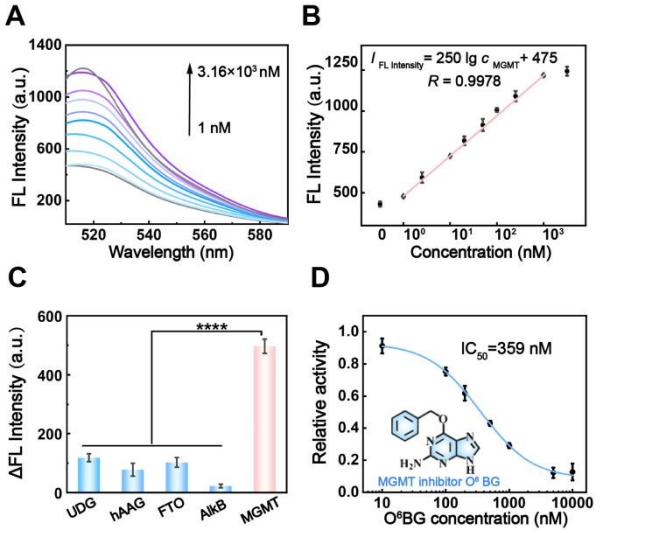

Fig. 4 Analytical performance of the Mr-TDF for monitoring MGMT activity. (A) Fluorescence response curves of Mr-TDF to MGMT from 0 nM to 3.16 × 10^3 nM in reaction buffer at 37 °C for 2 h. Fluorescence intensity as a function of MGMT concentration. (B) Calibration plot showing the linear correlation between fluorescence intensity and MGMT concentrations. Data at 0 nM and $10^{3.5}$ nM are shown as boundary references and excluded from fitting. Error bars are shown as mean ± SD (n = 3). (C) Histogram of ΔF ($I_{FAM} - I_{Blank}$) intensity in the presence of different interfering components: uracil DNA glycosylase (UDG), human alkyladenine DNA glycosylase (hAAG), m^6A demethylases (FTO and AlkB). The concentration for MGMT was 1 nM and all interferents were at 100 nM. Error bars are shown as mean ± SD (n = 3). The significant difference was calculated via Student's *t* test. ****P < 0.0001. (D) Change of relative MGMT activity in response to increasing concentrations of O^6-BG in reaction buffer at 37 °C for 2 h. Inset: chemical structure of O^6-BG. Error bars represent mean ± SD (n = 3).

Intracellular Imaging of MGMT for Distinguishing Chemoresistant Tumor Cells

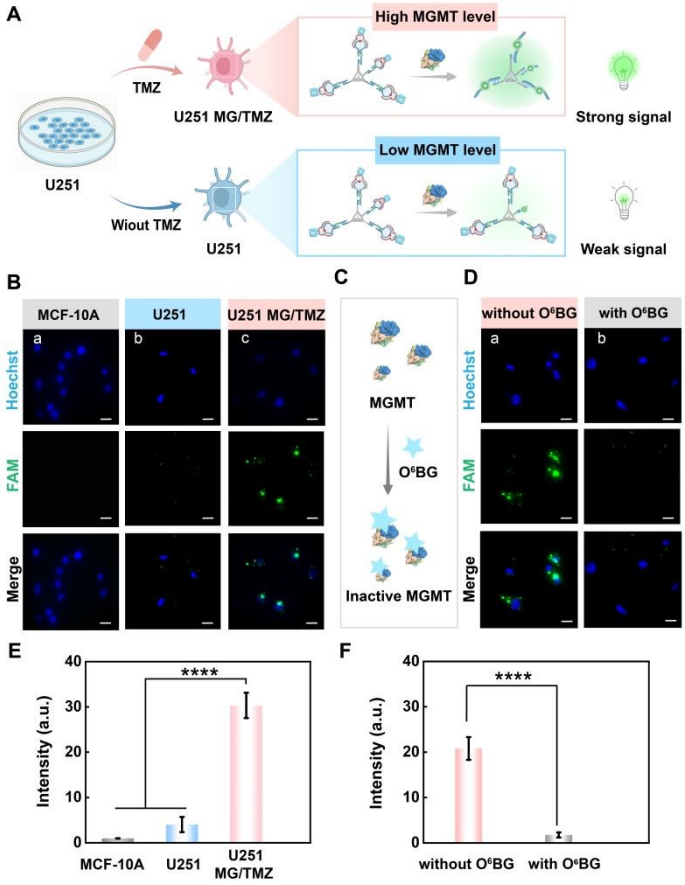

Fig. 5 Intracellular imaging of MGMT activity by Mr-TDF. (A) Schematic diagram of the Mr-TDF system for distinguishing chemoresistant cells based on MGMT activity. (B) Confocal fluorescence images of normal cells (MCF-10A), glioblastoma cells (U251) and temozolomide-resistant glioblastoma cells (U251 MG/TMZ) pretreat with Mr-TDF. Scale bar, 20 μm. (C) Schematic illustration of MGMT activity inhibited by O^6-BG. (D) Confocal fluorescence images of U251 MG/TMZ cells with or without O^6-BG pretreatment. Scale bar, 20 μm. (E, F) Statistical histogram of mean fluorescence intensities in the FAM channel from Figure 5B (E) and Figure 5D (F). Error bars are shown as mean ± SD (n = 3), where n denotes three independent biological replicate experiments. Approximately 50-80 cells per dish were analyzed to ensure representativeness. The significant difference was calculated via Student's *t* test. ****$P < 0.0001$.

To assess the capability of Mr-TDF for intracellular imaging of MGMT, representative cell lines varying MGMT expression levels were selected (Fig. 5A). Confocal fluorescence imaging was performed on these different cells after incubation with Mr-TDF (FAM channel) and nuclear dye (Hoechst channel). As shown in Fig. 5B, the fluorescence in FAM channel was faint in normal MCF-10A cells and slightly enhanced in chemosensitive U251 cells, but markedly stronger in chemoresistant U251 MG/TMZ cells. These observations were quantitatively corroborated by fluorescence intensity analysis, which revealed a more than 3-fold increase in the FAM channel signal in chemoresistant U251 MG/TMZ cells compared to U251 cells, with highly significant statistical differences ($P < 0.0001$, Fig. 5E). In addition, the imaging performance of free Mr probes and Mr-TDF was further compared in chemoresistant U251 MG/TMZ cells. The fluorescence signal from Mr-TDF was approximately 6.7 times stronger than that of free Mr probes (Fig. S6). Collectively, these results demonstrated that Mr-TDF effectively enables in situ imaging and discrimination of chemoresistant tumor cells from chemosensitive ones based on MGMT activity. To confirm that the intracellular fluorescent signal specifically arises from MGMT activity, the MGMT inhibitor O^6-BG was employed to suppress MGMT in U251 MG/TMZ cells (Fig. 5C). As illustrated in Fig. 5D, U251 MG/TMZ cells without O^6-BG treatment exhibited a distinct fluorescence signal in FAM channel. In contrast, the cells pre-treated with O^6-BG displayed a marked reduction in fluorescence. Quantitative analysis confirmed a highly significant difference in fluorescent intensity between O^6-BG-pretreated and untreated U251 MG/TMZ cells ($P < 0.0001$, Fig. 5F), further validating that the MGMTinduced fluorescence responses in chemoresistant tumor cell is mediated by Mr-TDF. Overall, these findings underscored the precision of Mr-TDF in distinguishing chemoresistant from chemosensitive tumor cells through sensitive monitoring of MGMT activity.

Conclusions

In conclusion, we presented a rationally designed fluorescent biosensor based on Mr-TDF, which enables high-sensitivity and dynamic in situ visualization of MGMT activity. This approach has demonstrated its efficacy as a rapid and reliable tool for distinguishing chemoresistant tumor cells in living cells. The nanoscale confinement of responsive modules within DNA frameworks not only enhances structural stability and response kinetics in complex biological environments, but also improves key analytical performance metrics, including linear detection range, detection limit, and sensitivity, thereby expanding its utility in MGMT activity-based bioanalysis. This advance facilitates precise discrimination of chemoresistant cells and effective screening of MGMT inhibitors, addresses a critical gap in monitoring chemoresistance. Together, the work described herein provides a versatile platform for probing resistance mechanisms and informing future therapeutic strategies.

Data availability

All the data supporting the findings of this study are available within the article and its ESI files† and from the corresponding author upon reasonable request.

Author contributions

X.Y. L.: investigation, formal analysis, writing-original draft; J.L.: funding acquisition, conceptualization, review & editing; X.M. Z.: conceptualization, investigation, writing; Y.M. L.: formal analysis, supervision; L.X. W.: investigation, formal analysis; D.P. J. and Y. Z.: funding acquisition, supervision, review & editing. All authors have given approval for the final version of the manuscript.

Conflicts of interest

There are no conflicts to declare.

Acknowledgements

We are grateful for financial support from the National Natural Science Foundation of China (22374123), and the Fundamental Research Funds for the Central Universities (SWU-XJLJ202303). We are grateful for the assistance of Y. Li (Analytical and Testing Center, Southwest University).

References

1 Tian, Y.; Wang, X.; Wu, C.; Qiao, J.; Jin, H.; Li, H. *Cancer Cell Int.,* 2024, **24**, 326.
2 Urso, L.; Uccelli, L.; Boschi, A.; Schillaci, O.; Filippi, L. *J. Nucl. Med.,* 2025, **66**, 344 − 348.
3 Holt, M. V.; Dou, Y.; Young, M. N.; Saltzman, A. B.; Anurag, M.; Lei, J. T.; Jain, A.; Leng, M.; Kim, B.-J.; Dobrolecki, L. E.; Faucher, S. F.; Savage, S.; Wang, C.; Shi, Z.; Villanueva, H.; Kremers, K.; Drinnon, K. D.; Castro, P. D.; Ittmann, M. M.; Khatani, M. M.; Kim, S. H.; Ellis, M. J.; Zhang, B.; Malovannaya, A.; Lerner, S. P. *Cell Rep. Med.,* 2025, **6**, 102255.
4 Zhang, Y.; Jiang, S.; He, F.; Tian, Y.; Hu, H.; Gao, L.; Zhang, L.; Chen, A.; Hu, Y.; Fan, L.; Yang, C.; Zhou, B.; Liu, D.; Zhou, Z.; Su, Y.; Qin, L.; Wang, Y.; He, H.; Lu, J.; Xiao, P.; Hu, S.; Wang, Q.-F. *Genome. Biol.,* 2023, **24**, 199.
5 Fletchera, N. M.; Belottea, J.; Saeda, M. G.; Memaj, I.; Diamondb, M. P.; Morrisc, R. T.;Saeda, G. M. *Free Radic. Biol. Med.,* 2016, **102**, 122–132
6 Liu, B.; Li, W.; Zhang, W.; Feng, C.; Wan, L.; He, S.; Xu, R.; Fu, Z.; Liu, Z.; Xu, H.; Jin, X.; Tu, C.; Li, Z. *Signal Transduct Target Ther.,* 2025, **10**, 165.
7 Emad, A.; Cairns, J.; Kalari, K. R.; Wang, L.; Sinha, S. *Genome Biol.,* 2017, **18**, 153.
8 Gouin, K. H., 3rd; Ing, N.; Plummer, J. T.; Rosser, C. J.; Ben Cheikh, B.; Oh, C.; Chen, S. S.; Chan, K. S.; Furuya, H.; Tourtellotte, W. G.; Knott, S. R. V.; Theodorescu, D. *Nat. Commun.,* 2021, **12**, 4906.
9 Dayanc, B.; Eris, S.; Gulfirat, N. E.; Ozden-Yilmaz, G.; Cakiroglu, E.; Coskun Deniz, O. S.; Karakulah, G.; Erkek-Ozhan, S.; Senturk, S. *Cell Death Dis.,* 2025, **16**, 414.
10 Peyraud, F.; Guégan, J.-P.; Rey, C.; Lara, O.; Odin, O.; Del Castillo, M.; Vanhersecke, L.; Coindre, J.-M.; Clot, E.; Brunet, M.; Grellety, T.; Tasseel, A.; Le Moulec, S.; Johnston, R. J.; Bessede, A.; Italiano, A. *Cell Reports Medicine*, 2025, **6**, 101934.
11 Kadioglu, O.; Saeed, M. E. M.; Mahmoud, N.; Azawi, S.; Mrasek, K.; Liehr, T.; Efferth, T. *Life Sciences*, 2021, **284**, 119601.
12 Pasyukova, E. G.; Symonenko, A. V.; Rybina, O. Y.; Vaiserman, A. M. *Ageing Res. Rev.,* 2021, **67**, 101312.
13 Fetahu, I. S.; Esser-Skala, W.; Dnyansagar, R.; Sindelar, S.; Rifatbegovic, F.; Bileck, A.; Skos, L.; Bozsaky, E.; Lazic, D.; Shaw, L.; Tötzl, M.; Tarlungeanu, D.; Bernkopf, M.; Rados, M.; Weninger, W.; Tomazou, E. M.; Bock, C.; Gerner, C.; Ladenstein, R.; Farlik, M.; Fortelny, N.; Taschner-Mandl, S. *Nat. Commun.*, 2023, **14**, 3620.
14 Duan, R.; Fu, Q.; Sun, Y.; Li, Q. *Ageing Res. Rev.*, 2022, **81**, 101743.
15 Zong, Z.; Hua, L.; Wang, Z.; Xu, H.; Ye, C.; Pan, B.; Zhao, Z.; Zhang, L.; Lu, J.; Liu, H.; Yu, R. *Drug Delivery*, 2019, **26**, 34 − 44.
16 Chen, Y.; Ding, K.; Zheng, S.; Gao, S.; Xu, X.; Wu, H.; Zhou, F.; Wang, Y.; Xu, J.; Wang, C.; Ling, C.; Xu, J.; Wang, L.; Wu, Q.; Giamas, G.; Chen, G.; Zhang, J.; Yi, C.; Ji, J. *Oncogene*, 2025, **44**, 1781 − 1792.
17 Lin, K.; Gueble, S. E.; Sundaram, R. K.; Huseman, E. D.; Bindra, R. S.; Herzon, S. B. *Science*, 2022, **377**, 502 − 511.
18 Kanugula, S.; Pegg, A. E. *Biochem. J.,* 2003, **375**, 449 − 455.
19 Daniels, D. S.; Mol, C. D.; Arvai, A. S.; Kanugula, S.; Pegg, A. E.; Tainer, J. A. *EMBO. J.,* 2000, **19**, 1719 − 1730.
20 Moon, B. S.; Cai, M.; Lee, G.; Zhao, T.; Song, X.; Giannotta, S. L.; Attenello, F. J.; Yu, M.; Lu, W. J. *Clin. Invest.,* 2020, **130**, 5782 − 5799.
21 Fan, C. H.; Liu, W. L.; Cao, H.; Wen, C.; Chen, L.; Jiang, G. *Cell Death Dis.*, 2013, **4**, e876.
22 Li, H.; Wu, Y.; Chen, Y.; Lv, J.; Qu, C.; Mei, T.; Zheng, Y.; Ye, C.; Li, F.; Ge, S.; Yao, A.; Jia, L. *Acta Neuropathol. Commun.,* 2025, **13**, 126.
23 Watson, A. J.; Sabharwal, A.; Thorncroft, M.; McGown, G.; Kerr, R.; Bojanic, S.; Soonawalla, Z.; King, A.; Miller, A.; Waller, S.; Leung, H.; Margison, G. P.; Middleton, M. R. *Clin. Cancer Res*., 2010, **16**, 743 − 749.
24 Tang, J.; Yang, R. *Cells*, 2025, **14**, 746.
25 McConnell, E. M.; Cozma, I.; Mou, Q.; Brennan, J. D.; Lu, Y.; Li, Y. *Chem. Soc. Rev.,* 2021, **50**, 8954-8994
26 Fan, H.; McGhee, C. E.; Lake, R. J.; Yang, Z.; Guo, Z.; Zhang, X.-B.; Lu, Y. *JACS. Au,* 2023, **3**, 1615 − 1622.
27 Cui, M.-R.; Li, X.-L.; Xu, J.-J.; Chen, H.-Y. *ACS Appl. Mater. Interfaces,* 2020, **12**, 13005 − 13012.
28 Shang, J.; Yu, S.; Li, R.; He, Y.; Wang, Y.; Wang, F. *Nano Lett.*, 2023, **23**, 1386 − 1394.
29 Zeng, W.-J.; Li, X.-R.; Liu, W.; Yuan, R.; Liang, W.-B.; Zhuo, Y. *Anal. Chem.,* 2024, **96**, 2117 − 2123.
30 He, Y.; Wang, Q.; Zhang, Q.; Wang, Y.; Jiang, Y.; Zhao, Q.; Liu, X.; Wang, F. *Small Methods,* 2025, **9**, 2401160.
31 Wang, X.; Yi, X.; Huang, Z.; He, J.; Wu, Z.; Chu, X.; Jiang, J. H. *Angew. Chem. Int. Ed.*, 2021, **60**, 19889 − 19896.
32 Ouyang, Y.; Zhang, P.; Willner, I. *Angew. Chem. Int. Ed.*, 2024, **63**, e202411118.
33 Huang, J.; Gambietz, S.; Sacca, B. *Small*, 2023, **19**, 2202253.
34 Chen, Z. P.; Zeng, W.; J.; Lei, Y.-M.; Liang, W.-B.; Yang, X.; Yuan, R.; Yang, C.; Zhuo, Y. *Angew. Chem. Int. Ed.,* 2025, **64**, e202414064.

View Article Online
DOI: 10.1039/D6SC01141A

All the data supporting the findings of this study are available within the article and its ESI files and from the corresponding author upon reasonable request.